Journal of
Nanoelectronics and Optoelectronics
Vol. 2, 222–233, 2007

REVIEW

Far-Infrared Characteristics of Bulk and Nanostructured Wide-Bandgap Semiconductors

Jiaguang Han, Abul K. Azad, and Weili Zhang*

School of Electrical and Computer Engineering, Oklahoma State University, Stillwater, Oklahoma 74078, USA

A review of far-infrared properties of popular bulk and nanostructured wide-bandgap semiconductors in the broadband terahertz region is presented. Such wide-bandgap semiconductor materials have shown promising applications in terahertz optoelectronics. The optical, dielectric or electric properties of bulk crystalline GaN, ZnO, and ZnS, and nanostructured ZnO and ZnS were characterized by terahertz time-domain spectroscopy measurements. Theoretical fitting based on dielectric models and effective medium models have shown good agreement with the measured results. The investigation reveals that the free-standing GaN exhibits a Drude-like behavior in the terahertz region, while the dielectric response of crystalline ZnO and ZnS is dominated by low-frequency transverse optical phonon modes. The ZnO tetrapod nanostructures exhibit very similar phonon resonances with that of single-crystal ZnO, whereas the phonon confinement in ZnS nanoparticles gave rise to a difference photon response compared to the bulk ZnS.

Keywords: Wide-Bandgap Semiconductors, Terahertz Time-Domain Spectroscopy, Bulk, Nanostructures, Phonons.

CONTENTS

1. INTRODUCTION

There has been an enormous interest in wide-bandgap semiconductors due to their large span of applications. In addition to the II–VI compounds zinc sulfide (ZnS), zinc selenide (ZnSe), zinc oxide (ZnO), cadmium sulfide (CdS), and etc., gallium nitride (GaN) and related III–V nitride materials continue to generate considerable excitement in semiconductors research with the success in fabricating short wavelength light emitting diodes, laser diodes, and novel transistors. The number of available wide-bandgap materials is still enlarging because of the recent progress in material growth technology that continuously introduces new semiconductor compounds.[1] As typical wide-bandgap semiconductors, GaN, ZnO, and ZnS have attracted growing interest owing to their fascinating physical and chemical properties and broad applications in photonics and optoelectronics. In particular, such compound semiconductors have been demonstrated to be excellent materials in terahertz (THz) optoelectronics, especially for high power THz pulse generation.[2–4] The understanding of their optical, dielectric, and electric properties over the broadband THz frequencies is essential for THz optoelectronic applications.

Epitaxial GaN, with wide-bandgap (∼3.4 eV), high breakdown field, large electron saturation velocity, and chemical stability at high temperatures, has been recognized as the excellent candidate material for short wavelength light emission and high power electronic applications. Recently, THz emission in nitride materials was observed with InGaN/GaN LED structures excited by the blue laser pulses from a frequency-doubled femtosecond Ti:sapphire laser.[2] It was observed that the THz emission showed strong dependence on bias voltage and excitation wavelength. The optical and electrical properties of nitride materials have been studied extensively at UV to blue, and infrared frequency ranges by a variety of techniques, such as photoluminescence, magneto-optical infrared

*Author to whom correspondence should be addressed.

 1555-130X/2007/2/222/012 doi:10.1166/jno.2007.302

transmission, infrared spectroscopic ellipsometry, and THz time-domain spectroscopy (THz-TDS).[2–12] The optical phonon modes in the frequency range of 300–1200 cm^{-1} in α-GaN have been determined at room-temperature by infrared ellipsometry measurement.[7] The complex conductivity and dielectric function of an n-type, 180-μm-thick, freestanding GaN crystal was characterized by THz-TDS transmission measurements, which revealed the frequency-dependent electron dynamics, power absorption and optical dispersion of GaN in a broad frequency range in the THz regime.[11]

As a direct band gap (3.37 eV at room temperature) compound, ZnO is one of the most promising semiconductors for electro-optic, acousto-optic, and optoelectronic devices applications.[13–16] It has also been demonstrated experimentally that ZnO shows significantly higher radiation hardness than Si, GaN, and GaAs.[17] ZnO is considered as a promising material for THz optics because of a number of advantages: ease in fabrication, wide bandgap, rather high mobility and resistivity, and transparent in a broad frequency range. Pulsed THz radiation has been demonstrated from a photoconductive switch fabricated on high-resistivity, single-crystal ZnO.[3] The experimental result indicated that the high breakdown electric field enables ZnO to be an intriguing semiconductor in high power THz generation. The infrared dielectric function and the optical phonon modes of high-resistivity single-crystal ZnO were investigated using ellipsometry, Raman scattering, and THz-TDS measurements over the broad far-infrared frequency range.[16, 18]

Nanostructured ZnO has promising photoelectronic, photochemical, and catalytic properties and potential

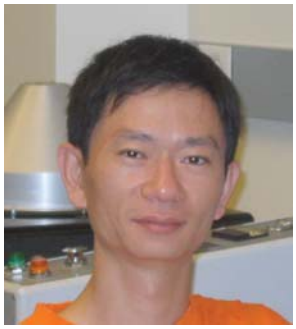

Jiaguang Han received his B.S. degree in Material Physics from Beijing Normal University, in 2000, and Ph.D. degree in Applied Physics from Shanghai Institute of Applied Physics, Chinese Academy of Sciences, in 2006. He was a visiting researcher at the Japanese High Energy Accelerator Research Organization in 2004 and 2005. In 2006, he received the Einstein Awards from the Embassies of Germany and Switzerland, and was invited to visit the German and Swiss universities and research institutes. Currently, he works as a Postdoctoral fellow in the School of Electrical & Computer Engineering at Oklahoma State University.

Abul K. Azad received his M.S. and Ph.D. degrees in Electrical and Computer Engineering from the Oklahoma State University in 2003 and 2006, respectively. Since June 2006 he works as a Postdoctoral Research Associate in the Department of Physics, Applied Physics, and Astronomy at Rensselaer Polytechnic Institute. Currently, he is with Los Alamos National Laboratory. Dr. Azad's research interests are in the area of terahertz (THz) optoelectronics and ultrafast properties of materials. He contributed to the investigation of carrier and phonon dynamics of a variety of materials from bulk to nanostructured semiconductors. His research also includes surface plasmon polaritons, metamaterials, and photonic crystals in the THz frequency range. He has authored more than 10 journal publications. He is a member of the Optical Society of America.

Weili Zhang received his B.S. degree in laser science, and the M.S. and Ph.D. degrees in optical engineering from Tianjin University, in 1987, 1990, and 1993, respectively. From 1993 to 1995, he worked as a postdoctoral research associate in the Department of Physics at the Hong Kong University of Science & Technology. In 1995, he joined the faculty in Department of Optoelectronics Technology at Tianjin University. In 2000, he worked as a Visiting Associate Professor in the Ultrafast THz Research Group at Oklahoma State University (OSU). Currently he is Associate Professor in the School of Electrical and Computer Engineering at OSU. His research interests have included terahertz optoelectronics, ultrafast lasers and phenomena, nanostructured and microstructured material optics, and semiconductor processing. He contributed to the investigation of terawatt femtosecond pulse amplification, THz plasmonics, THz metamaterials, and THz properties of wide-bandgap semiconductors and nanostructures. He has authored or co-authored 110 peer-reviewed journal papers. He is a committee member of the conference for Terahertz physics, devices, and systems at Optics East 2006 and 2007. He is Associate Editor of the Journal of Optoelectronics and Lasers, and member of Editorial Committee of Optoelectronics Letters and Chinese Optics Letters. He is a member of the American Physical Society, the Institute of Electrical and Electronics Engineers, and the Optical Society of America.

applications in piezoelectric transduction, optical emission, catalysis, actuation, drug delivery, spintronics, and optical storage.[19–23] Various one-dimensional structures of ZnO, such as tetrapods, nanowires and nanobelts have attracted much attention in recent years.[20] In particular, the ZnO tetrapod structures are expected to exhibit special characteristics due to single-crystalline structure and controllable morphology.[21] It was reported that ZnO tetrapods are a good choice for gas sensors for sensitive response to ethanol and methane at different levels and temperatures.[22]

ZnS is an II–VI compound with a wide-band gap of 3.6 eV at room temperature. It is an essential material for cathode-ray tube luminescent materials, electroluminescence, solar cells, and UV semiconductor lasers for optical lithography.[24, 25] ZnS is also an excellent optical material in the infrared and far-infrared regions owing to the low absorption, it thus can be used as infrared windows and lenses. Nanostructured ZnS, synthesized by various chemical methods, has potential applications in nonlinear optical devices and fast optical switches.[26, 27] It exhibits strong size effect in the nanometer regime. Recently, the nature of vibrations of ZnS nanoparticles has received much attention. The surface optical modes of ZnS nanoparticles were characterized in the spectral range 100–700 cm^{-1}.[28]

In this article, we review the far-infrared optical and complex dielectric function of crystalline wide bandgap semiconductors GaN, ZnO, and ZnS, and nanostructured ZnO and ZnS characterized by THz-TDS measurements.[29] The experimental results were analyzed by theoretical dielectric models that provided good agreement and interpretation to the measured complex conductivity, optical phonon resonances, and dispersion properties.

2. EXPERIMENTAL METHODS

2.1. THz-TDS System

The samples were characterized by use of a broadband, photoconductive switch-based THz-TDS system, in which the THz beam was collimated by an 8-F confocal geometry.[11, 30] A self-mode-locked Ti:sapphire laser capable of generating ultrafast pulses with FWHM duration of tens of femtoseconds is used as the gating source. While this 8-F configuration enables an excellent THz beam coupling between the transmitter and the receiver, a frequency-independent 3.5-mm-diam THz beam waist is achieved which favors the characterization of samples of small dimensions. The THz-TDS system has a useful bandwidth of 0.1 to 4.5 THz (3 mm–67 μm) and a signal to noise ratio (S/N) of >10000:1. The transmitted time-domain THz pulses and the corresponding spectra of the reference are obtained simultaneously. In order to further increase the S/N of measurements, each curve is an average of six individual scans.

2.2. THz-TDS of Bulk Semiconductors

For the bulk samples, the measurements were directly performed with the sample attached on a well-defined optical aperture.[11, 18, 30] The transmitted electric field of THz pulses through the sample and the reference are recorded in time domain and the corresponding frequency spectra are obtained by numerical Fourier-transform. Due to limited thickness of the samples, the main transmitted THz pulse is trailed by multiple-reflected pulses in time domain. However, the clean separation between the main transmitted pulse and the first internal reflection enabled data analysis on the main transmitted pulse only. The complex spectrum of the sample pulse $E_2(\omega)$ can be extrapolated in terms of reference spectrum $E_1(\omega)$ and the transfer function as,[11]

$$\frac{E_2(\omega)}{E_1(\omega)} = t_{12}t_{21}\exp[id(k-k_0)]\exp(-\alpha d/2) \quad (1)$$

where, t_{12} and t_{21} are frequency-dependent complex Fresnel transmission coefficients, d is the sample thickness, α is power absorption, $k = 2\pi n_r/\lambda$ and $k_0 = 2\pi/\lambda$ are the propagation wavevectors, respectively, and n_r is refractive index of the sample. The frequency-dependent effective complex dielectric response of sample is determined by the recorded data of power absorption and refractive index through the relationship: $\varepsilon(\omega) = (n_r + in_i)^2$, while the imaginary part of the refractive index n_i is related to the power absorption as $n_i = \alpha\lambda/4\pi$. As a result, the real and the imaginary part of the dielectric function are given as $\varepsilon_r = n_r^2 - (\alpha\lambda/4\pi)^2$ and $\varepsilon_i = \alpha n_r\lambda/2\pi$, respectively.[30]

2.3. THz-TDS of Nanostructured Semiconductors

The powder-form nanostructured samples were contained in a silicon cell that attached to a well-defined aperture. In the transmission experiments, two identical hand-made cells with dimensions of 25 mm × 16 mm, and spacer thickness of 0.42 mm were employed; one for sample and the other one for reference. The cells were made of 636-μm-thick, high-quality silicon slabs (p-type resistivity, 20 Ω cm). The complex transmission spectra of the reference $E_1(\omega)$ and the sample $E_2(\omega)$ are given by

$$E_1(\omega) = E_0(\omega)t_{sa}t_{as}\exp(ik_0d) \quad (2)$$

$$E_2(\omega) = E_0(\omega)t_{sn}t_{ns}\exp[id(k-k_0)]\exp(-\alpha d/2) \quad (3)$$

where $E_0(\omega)$ is the incident pulse spectrum, t_{sa}, t_{as}, t_{sn}, and t_{ns} are the Fresnel transmission coefficients of the THz pulses propagating through Si-air, air-Si, Si-sample, and sample-Si interfaces, respectively, given by $t_{sa} = 2n_s/(1+n_s)$, $t_{as} = 2/(1+n_s)$, $t_{sn} = 2n_s/(n_s+n_r)$, and $t_{ns} = 2n_r/(n_s+n_r)$, and n_s and n_r are refractive indices of silicon and the nanostructures. The frequency-dependent absorption and dispersion of the samples were obtained using the Fourier analysis of the input and output pulses as described above.

3. THEORY

3.1. Dielectric Model

In the THz regime, the dielectric function of samples usually is described by the dielectric model. Generally, the total dielectric function $\varepsilon_m(\omega)$ consists of contributions from the high-frequency dielectric constant, conduction free electrons, and lattice vibrations/optical phonons:[31–34]

$$\varepsilon_m(\omega) = \varepsilon_\infty - \frac{\omega_p^2}{\omega^2 + i\gamma\omega} + \sum_j \frac{\varepsilon_{st_j}\omega_{TO_j}^2}{\omega_{TO_j}^2 - \omega^2 - i\Gamma_j\omega} \quad (4)$$

The first term ε_∞ is the high-frequency dielectric constant, the second term describes the contribution of free electrons or plasmons, and the third term is a contribution form optical phonons. The key parameters describing the dynamics of free electrons or plasmons in a semiconductor are plasma frequency $\omega_p = [Ne^2/(\varepsilon_0 m^*)]^{1/2}$ and carrier damping constant γ, where N is the carrier density, m^* is the electron effective mass and ε_0 is the free-space permittivity constant with value 8.854×10^{-12} F/m. The mobility can be obtained from $\mu = e/(m^*\gamma)$. In the optical phonon term, the summation is over all lattice oscillations with the jth transverse optical frequency ω_{TO_j}, oscillator strength ε_{st_j}, and phonon damping constant Γ_j. Two most commonly used models can be extracted from Eq. (4). When the response mainly originates from the contribution of free electrons or plasmons, we usually adopt Drude model as

$$\varepsilon_m(\omega) = \varepsilon_{mr} + i\varepsilon_{mi} = \varepsilon_\infty - \frac{\omega_p^2}{\omega^2 + i\gamma\omega} \quad (5)$$

where ε_{mr} and ε_{mi} are the real and imaginary parts of dielectric function. The dielectric properties of metals and semiconductors usually well described by the Drude model.

On the other hand, if the interaction of a radiation field with the fundamental lattice vibration plays a dominating role and results in absorption of electromagnetic waves due to the creation or annihilation of lattice vibration, the dielectric function $\varepsilon_m(\omega)$ can be expressed by the classical pseudo-harmonic phonon model with the first approximation

$$\varepsilon_m(\omega) = \varepsilon_{mr} + i\varepsilon_{mi} = \varepsilon_\infty + \frac{\varepsilon_{st}\omega_{TO}^2}{\omega_{TO}^2 - \omega^2 - i\gamma\omega} \quad (6)$$

The optical responses of crystals are mostly well described within such a framework of phonon theory.

3.2. Effective Medium Model

The powder-form nanostructures contained in the silicon cells are a composite medium of nanostructures and air. In this case, the THz-TDS measurements are a result of the two-phase-mixtured composite. Hence, the optical properties of composite materials are often characterized by effective-medium theory (EMT), in which electromagnetic interactions between pure materials and host matrices are approximately taken into account.[35] Among all the EMT approaches, the Maxwell-Garnett (MG) model, Bruggeman (BR) model, and simple effective medium model are most commonly used. Here we briefly discuss these three models. The MG effective dielectric function can be extracted through the relation

$$\frac{\varepsilon_{eff} - \varepsilon_h}{\varepsilon_{eff} + 2\varepsilon_h} = f\frac{\varepsilon_m - \varepsilon_h}{\varepsilon_m + 2\varepsilon_h} \quad (7)$$

where ε_{eff}, ε_h and ε_m are dielectric constants of the effective medium, the host medium, and the pure sample, respectively, f is a filling factor that defines the volume ratio of pure sample and the whole cell. The MG model involves interactions between the particles only through the Lorentz filed, which limits its use to small filling factors.[36] MG approach describes an isotropic matrix containing spherical inclusions that are isolated from each other, such as the metal particles dispersed in a surrounding host matrix.

The BR model accounts for certain correlations due to self-consistent determination of dielectric properties.[37] In this theory, two elements are treated equally and their properties are determined self-consistently, making it a typically self-consistent model. The effective dielectric function for a two-phase system is obtained by solving the BR equation

$$f\left(\frac{\varepsilon_m - \varepsilon_{eff}}{\varepsilon_m + 2\varepsilon_{eff}}\right) + (1-f)\left(\frac{\varepsilon_h - \varepsilon_{eff}}{\varepsilon_h + 2\varepsilon_{eff}}\right) = 0 \quad (8)$$

The simple effective medium model describes the distribution of two elements through a volume filling fraction

$$\varepsilon_{eff}(\omega) = f\varepsilon_m(\omega) + (1-f)\varepsilon_h \quad (9)$$

The detailed discussions about these three models, for instance the validity or the application, have been described extensively elsewhere.[35]

4. RESULTS AND DISCUSSIONS

4.1. Crystalline Wide-Bandgap Semiconductors

4.1.1. Gallium Nitride

The GaN sample is an unintentionally n-doped, 5 mm × 5 mm × 180-μm-thick, freestanding crystalline plate. Originally grown on C-plane sapphire by hydride-vapor-phase epitaxy, the GaN layer was removed from the sapphire substrate by laser liftoff.[2] The c-axis is perpendicular to the main planes of the sample. The measured THz pulses transmitted through the sample and reference apertures are shown in Figure 1(a).[11] The peak amplitude of the first transmitted output pulse is about 30% that of the reference

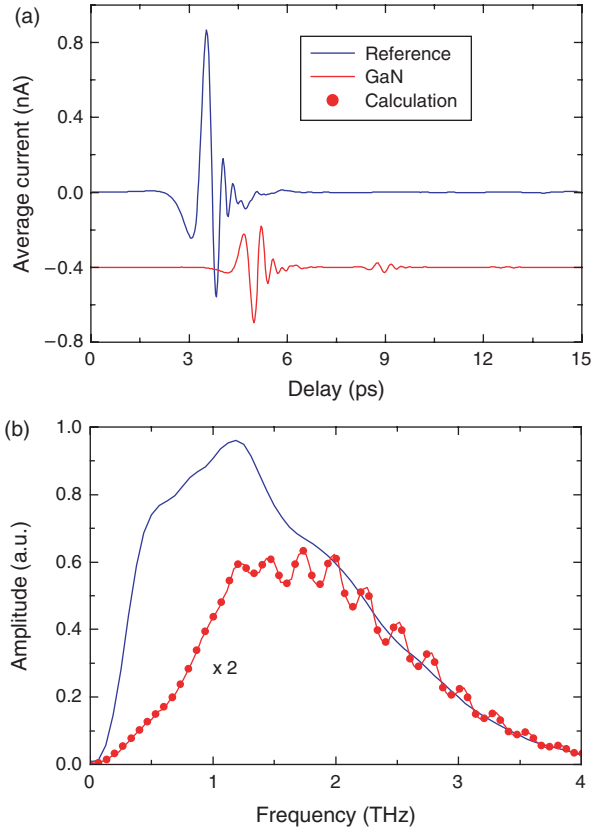

Fig. 1. (a) THz-TDS measured reference pulse and sample pulse with reflections (vertically displaced by −0.4 nA) for free-standing GaN; (b) Fourier-transformed amplitude spectra of the reference and sample (multiplied by 2×) pulses. The dots represent the calculated sample spectrum from the reference.

input pulse due to the frequency-dependent absorption and reflection by the GaN plate. The additional pulses are due to multiple reflections by of the sample. Figure 1(b) illustrates the corresponding normalized amplitude spectra of the input pulse and the output pulse train (multiplied by 2×). The oscillation in the output spectrum is due to multiple reflections and is described by the well-known amplitude transmission function of a parallel dielectric slab.[38]

The frequency-dependent dielectric constant is defined as $\varepsilon = \varepsilon_\infty + i\sigma/(\omega\varepsilon_0) = (n_r + in_i)^2$, where σ is the complex conductivity. Using this relationship the real and imaginary conductivity shown in Figure 2(b) were obtained from the experimentally determined α and n curves shown in Figure 2(a).[11] The measured absorption, index of refraction and complex conductivity were then theoretically fit using the simple Drude model of Eq. (5), for which the complex conductivity is defined by $\sigma = i\varepsilon_0\omega_p^2/(\omega + i\gamma)$. Three parameters were used to fit the experimental data: the plasma frequency $\omega_p/2\pi =$ 1.82 THz, the carrier damping rate $\gamma/2\pi = 0.81$ THz, and the real part of dielectric constant $\varepsilon_\infty = 9.4$. Given the reduced mass $m^* = 0.22\ m_0$ for electrons in GaN,[10] these parameters correspond to a number density of $N = 0.91 \times 10^{16}/\text{cm}^3$ and a mobility $\mu = 1570\ \text{cm}^2/\text{Vs}$. The

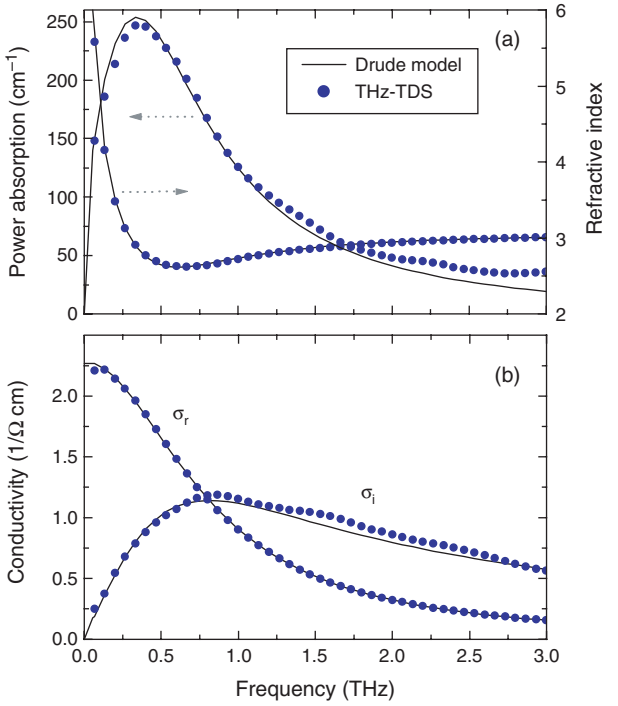

Fig. 2. Comparison of measured results of GaN with Drude model fitting. (a) Power absorption coefficient α and the real part of refractive index n_r; (b) complex electric conductivity σ_r and σ_i.

free carriers in this crystalline GaN are dominated by O donors over Si donors.[9] In Figure 2(a), the material absorption of intrinsic GaN, determined by the imaginary part of the dielectric constant, is responsible for the difference between the Drude fitting curve and our measurement of power absorption at frequencies higher than 2 THz. The measured real part of refractive index n_r shown in Figure 2(a) agrees quite well with Drude fitting. The real and imaginary electric conductivity calculated from the optical data are shown in Figure 2(b) respectively, where Drude model provides good fit on the measurements.

In addition, the low-frequency (<1.0 THz) electric response of crystalline GaN was further characterized by a modified THz-TDS system that operates in a low-frequency range of 0.05–1.0 THz.[11] Using the same parameters $\omega_p/2\pi = 1.82$ THz, $\gamma/2\pi = 0.81$ THz, and $\varepsilon_\infty = 9.4$ as that in Figure 2, the same Drude fitting shows excellent agreement with the low-frequency measurements, verifying the accuracy of the broad-band THz-TDS results.

4.1.2. Zinc Oxide

The ZnO sample is an undoped, 5 mm × 5 mm × 0.5-mm-thick, freestanding single crystal (obtained from MTI Corporation, USA). The both side polished plate has a crystal orientation ⟨0001⟩ with c-axis perpendicular to the surface. Hydrothermal growth method was used to fabricate the wurtzite, high-resistivity ZnO with purity higher than 99.99%.

Based on the THz-TDS transmission measurements, the experimentally extracted power absorption $\alpha(\omega)$ and the refractive index $n(\omega)$ of single-crystal ZnO are plotted in Figure 3 over the frequency range of 0.3–3.0 THz.[18] The power absorption increases with increasing frequency and no prominent absorption peaks are observed below 3.0 THz. This can be verified by the measured refractive index which shows no remarkable features. Employing the measured data of power absorption and refractive index, we obtain the frequency-dependent complex dielectric function. In Figure 4, the real dielectric constant shows a feature that is essentially the square of the refractive index n_r because the absorption by the sample is small in the spectral region concerned and the contribution of the absorption coefficient to the real dielectric constant is nearly negligible.[18]

Within the framework of the pseudo harmonic model by Eq. (6), the recorded data agree well with the theoretical fitting. Three parameters are used to fit the experimental data: $\varepsilon_0 = 7.77$, $\omega_{TO}/2\pi = 12.42$ THz and $\gamma/2\pi = 0.82$ THz. Given the high-frequency dielectric constant $\varepsilon_\infty = 3.705$,[39] this theoretical calculation presents well fit on the THz-TDS measurements as shown in Figures 3 and 4. Therefore, the presence of a dominant TO-phonon resonance centered at $\omega_{TO}/2\pi = 12.42$ THz with a linewidth of $\gamma/2\pi = 0.82$ THz and a strength $\varepsilon_{st} = \varepsilon_0 - \varepsilon_\infty = 4.065$ is well-determined.

Such a TO phonon resonance agrees well with previous measurements.[40–43] As one of the II–VI compounds,

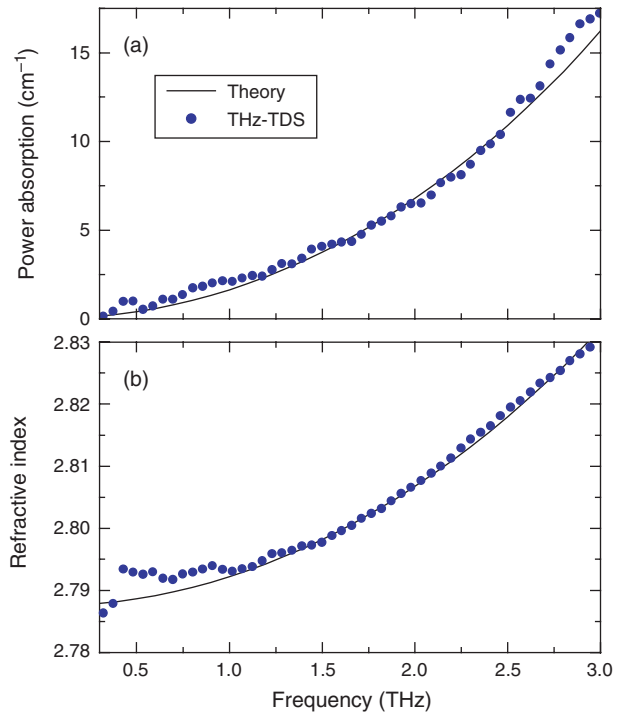

Fig. 3. (a) Comparison of measured power absorption α with that obtained from pseudo-harmonic theoretical fitting for single-crystal ZnO; (b) measured refractive index and the theoretical fitting.

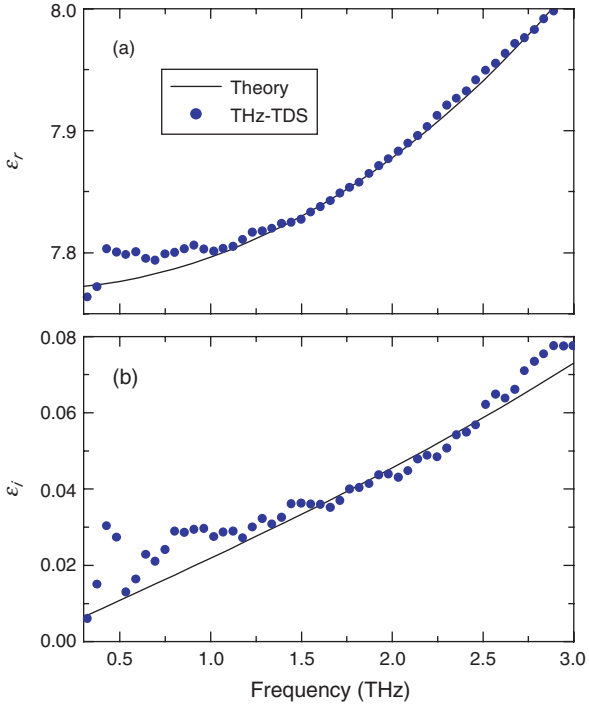

Fig. 4. Complex dielectric constant of single-crystal ZnO: (a) measured real part of dielectric constant ε_r and the theoretical fitting; (b) measured imaginary dielectric constant ε_i and the theoretical fitting.

wurtzite ZnO belongs to the $C_{6v}^4(P6_3mc)$ space group. There are four atoms per unit cell, leading to twelve phonon branches: nine optical and three acoustic. Group theory predicts the existence of the following optical modes:[44, 45] an A_1 branch, an E_1 branch, two E_2 branches, and two silent B_1 modes. The A_1 and E_1 are both Raman active and infrared active, while E_2 is Raman active only. In addition, the infrared-active A_1 and E_1 branches split into longitudinal optical (LO) and transverse optical component. The previous infrared reflectivity measurement indicated that the frequency of the TO (E_1) was located at 414 cm^{-1} (12.42 THz),[43] and the later Raman spectrum also observed that such a TO (E_1) is located at 413 cm^{-1} (12.40 THz).[40] The extrapolation based on the fitting of our experimental results gives a better agreement with this typical value.

Our result is further confirmed by the estimation of the frequency of LO (E_1). It is known that the frequency of LO (E_1) can be estimated from the well-known Lyddane-Schs-Teller relationship, $\omega_{LO}^2/\omega_{TO}^2 = \varepsilon_0/\varepsilon_\infty$. Using the above fitting parameters, we obtain the frequency of LO (E_1) as $\omega_{LO}/2\pi = 599$ cm^{-1} (17.98 THz). Compared to the reported experimental value 591 cm^{-1}, such a theoretical estimation is reliable.

4.1.3. Zinc Sulfide

The single-crystal ZnS sample is an undoped, 10 mm × 10 mm × 1 mm-thick, ⟨100⟩ oriented, freestanding plate

optically polished on both sides (RMT Ltd, Russia). It was grown from a source of polycrystalline ZnS at temperature of 1100–1250 °C and a pressure of 1 atm in a hydrogen-filled ampoule by the seeded vapor-phase free growth technology. Growth was along the ⟨111⟩ direction, and the crystal consists of 96–98% zincblende and 2–4% Wurtzite structures. The resistivity of the crystal is in the range of 10^8–10^{12} Ω cm.

The experimentally extracted power absorption of single-crystal ZnS is plotted in Figure 5(a).[30] Three prominent resonance lines are observed at 0.78, 2.20, and 2.80 THz, respectively, and are well assigned based on the previous predictions or observations.[4, 46–51] The first resonance peak, centered at 0.78 THz, has lifted the absorption coefficient to 2 cm^{-1}. In the Raman measurements this peak was interpreted as a superposition of two difference phonon bands, LA-TA and LO-TO.[46] These phonons were calculated at 88, 110, 306, and 333 cm^{-1} for the TA, LA, TO, and LO modes, respectively. The second and broad resonance line with peak power absorption coefficient of 11 cm^{-1} is located at 2.20 THz. It is referred to as the transverse TA (L) phonon connecting to two-phonon generation processes of acoustic phonons and was verified with neutron scattering measurements.[47–49] The resonance feature at 2.80 THz, showing peak absorption of 20 cm^{-1}, was previously observed to be one of the critical-point mode frequencies by neutron scattering measurements at room temperature.[50] It was defined as the TA (X) phonon and was considered as one of the four characteristic zone-boundary phonons used to describe the three-phonon processes in cubic ZnS.[51] In comparison with previous measurements the dots show the room temperature absorption data in the frequency range of 1.0–2.2 THz by channel spectrum technique.

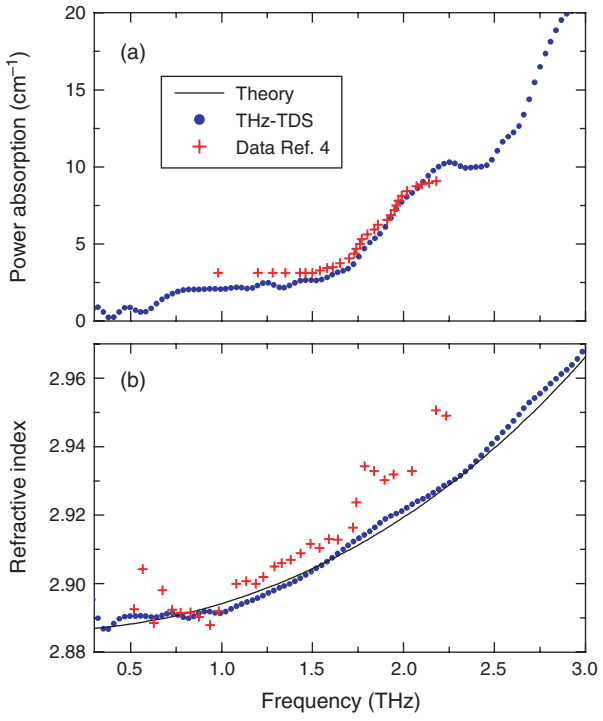

Fig. 5. (a) Comparison of measured results for the absorption of single-crystal ZnS with: the data from Ref. [4]; (b) comparison of measured refractive index of single crystal ZnS with: the values calculated using the damped harmonic oscillator model and the data from Ref. [4].

Figure 5(b) illustrates the frequency-dependent refractive index of single-crystal ZnS. Clearly, the measured result also reveals the effect of the phonon resonances shown in the power absorption. Similar to ZnTe, the refractive index increases with increasing frequencies.[52] This feature is dominated by a high-frequency TO-phonon resonance as predicted in early work. However, compared to the experimental data of ZnTe, the increase in the refractive index of ZnS is not very sharp since the TO-phonon line is centered at 8.13 THz, much higher than 5.32 THz, at which the TO phonon is located for ZnTe. The measured refractive index is theoretically fit using the dielectric response of a damped harmonic oscillator.

The frequency-dependent dielectric constant in the infrared region for the harmonic oscillator is formulated as Eq. (6). In Figure 5(b) the theoretical fitting to the measured index n is shown with the TO-phonon resonance centered at $\omega_{TO}/2\pi = 8.13$ THz with a linewidth of $\gamma/2\pi = 0.025$ THz, optical dielectric constant $\varepsilon_\infty = 5.13$, and the TO-phonon strength $\varepsilon_{st} = 3.19$. The good agreement between the measured data and fitting verifies the dominance of the TO-phonon resonance shown on the refractive index curve. The power absorption was also fit to the TO-phonon line at 8.13 THz, however, it shows a very weak effect compared to these observed TA-phonon resonance features as well as the LA phonons around 5.80 THz. The refractive index of ZnS at various temperatures in the range of 17–74 cm^{-1} (0.5–2.2 THz) has been studied previously by using channel spectrum technique.[48, 49] We plot the previous data at room temperature (crosses) for comparison. It was fit with an undamped harmonic oscillator using parameters $\omega_{TO}/2\pi = 7.80$ THz, $\varepsilon_\infty = 4.7$, and $\varepsilon_0 = \varepsilon_\infty + \varepsilon_{st} = 8.34$.[4] Obviously, our results show a better correlation with the theoretical fit and demonstrate the efficiency of THz-TDS characterizations and the accuracy with which it determines the optical and dielectric parameters of the measured sample.

Based on the measured data of power absorption and refractive index we have extracted the frequency-dependent complex dielectric function of single-crystal ZnS as shown in Figure 6.[30] The real dielectric constant shows a feature that is essentially the square of the refractive index n_r. This is because the absorption by the sample is small in the spectral region concerned and the contribution of the absorption coefficient to the real dielectric constant is nearly negligible. The plot of the imaginary dielectric constant shown in Figure 6(b) has features similar to the power absorption curve but reveals the phonon resonance peaks more clearly. It therefore provides further

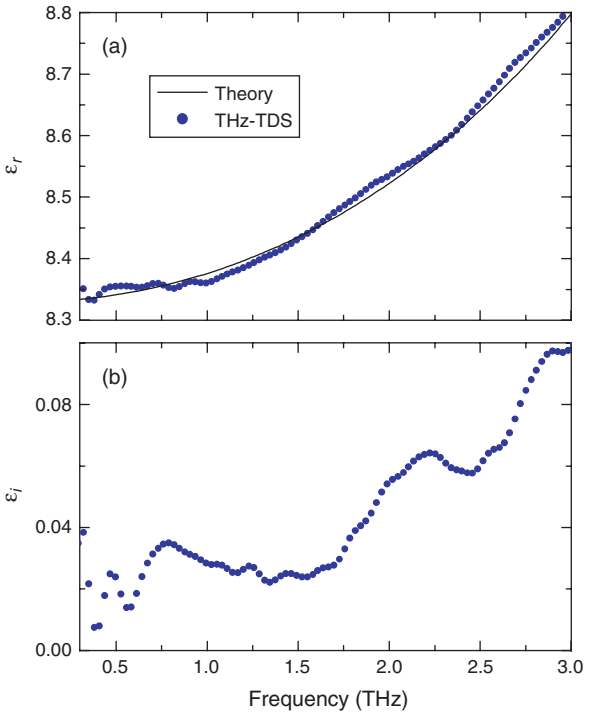

Fig. 6. Complex dielectric constant of single-crystal ZnS: (a) measured real part of dielectric constant ε_r and the theoretical fitting; (b) measured imaginary dielectric constant ε_i.

verification of the phonon resonances determined by the power absorption and refractive index.

4.2. Nanostructured Wide-Bandgap Semiconductors

4.2.1. ZnO Tetrapods

The ZnO tetrapods were grown by the vapor phase transport method by heating the Zn powder to 700 °C in a quartz tube furnace at ambient pressure while purged with argon gas.[53] The individual tetrapod structures were isolated by sonicating them in methanol. Scanning electron microscope and optical microscope were used to characterize the shape and the size of the tetrapods, and X-ray diffraction revealed the hexagonal wurtzite structures. The diameter of the legs was estimated to be between 200 and 800 nm while the length of the legs was between 10–30 μm.

The THz-TDS determined frequency-dependent power absorption coefficient $\alpha(\omega)$ and the refractive index $n(\omega)$ are plotted in Figure 7.[53] The measured power absorption increases as a function of frequency and no prominent absorption peak is observed below 3.5 THz, whereas the refractive index approaches a constant of 1.03. The measured complex dielectric constant of the ZnO tetrapods extracted from the data of power absorption and refractive index are illustrated Figure 8.[53] Since the sample to be measured is loosely packed ZnO tetrapods and consists of both ZnO tetrapods and air, the dielectric constant in Figure 8 is the effective complex dielectric constant ε_{eff},

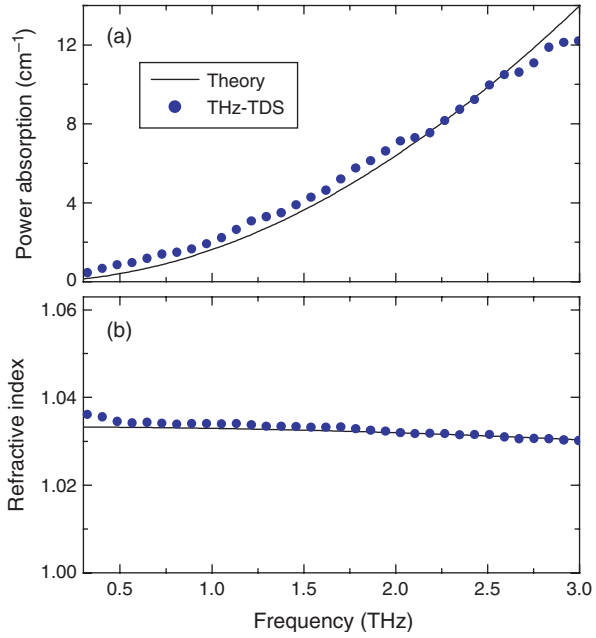

Fig. 7. THz-TDS measured results and the theoretical fitting for ZnO tetrapods: (a) power absorption $\alpha(\omega)$; (b) refractive index $n(\omega)$.

with the contributions from both the air and the pure ZnO tetrapods. The simple effective medium theory described by Eq. (9) was employed to obtain the effective dielectric function of ZnO tetrapods, where the filling factor f defines the volume fraction of the tetrapods and was measured during the experiment. The dielectric constants of the host medium, in our case is air, $\varepsilon_h = \varepsilon_{air} = 1.0$. The frequency-dependent dielectric function of the pure ZnO tetrapods $\varepsilon_m(\omega)$ can be determined by Eq. (6).

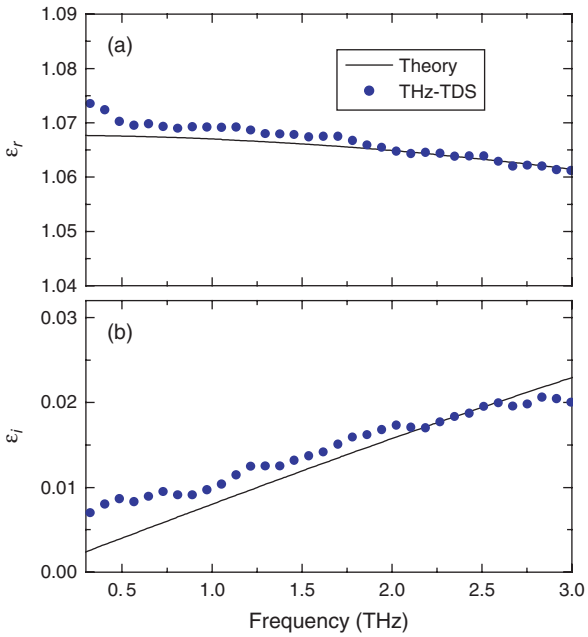

Fig. 8. Frequency-dependent complex dielectric function of the composite ZnO tetrapods (a) real part $\varepsilon_r(\omega)$, and (b) imaginary part $\varepsilon_i(\omega)$.

One can achieve a best fit on the experimental data with following parameters: $f = 0.01736$, $\varepsilon_\infty = 1.50$, $\varepsilon_{st} = 3.40$, $\omega_{TO}/2\pi = 12.41 \pm 0.2$ THz, $\gamma/2\pi = 21.0 \pm 0.2$ THz. The fitting of power absorption and refractive index in Figure 7 is based on the same parameters. The fitting reveals the presence of a dominant TO-phonon resonance of ZnO tetrapods centered at $\omega_{TO}/2\pi = 12.41$ THz with a phonon damping constant $\gamma/2\pi = 21.0$ THz and a strength $\varepsilon_{st} = 3.40$. Such a TO mode at 12.41 THz is a typical transverse optical mode in the bulk ZnO of wurtzite structure with the assignment E_1(TO).[40, 54] If τ is the TO phonon lifetime we have $\tau = 1/\gamma$ with value $\tau = 7.6$ fs. Actually, τ depends very critically on the type of phonon scattering mechanism and different scattering laws usually define the diverse lifetime. The obtained TO phonon lifetime τ results mainly from the calculation of absorption in which scattering from transverse optical phonon has been considered.

Figure 9 shows the power absorption and refractive index of the pure ZnO tetrapods, extracted using the pseudo harmonic model by Eq. (6) and the simple EMT model Eq. (9), in comparison with that of bulk single-crystal ZnO and the tetrapod-air composite samples.[53] The THz spectra of bulk single-crystal ZnO exhibit similar behaviors as that of the ZnO tetrapod media. The pure ZnO tetrapods represent the obviously higher power absorption than that of the composite tetrapods and the bulk single-crystal ZnO. The refractive index of the pure ZnO tetrapods, 2.21 is close to the value, 2.80 of the bulk single-crystal ZnO, but much larger than 1.03, the value for the measured composite tetrapod medium. It shows that the THz spectrum of the bulk single-crystal ZnO is also dominated by the E_1 (TO) phonon mode centered at the frequency 12.42 THz. All of these features indicate that the ZnO tetrapod structures reveal quite similar phonon response characteristics as the bulk single-crystal ZnO in the low-frequency THz regime.

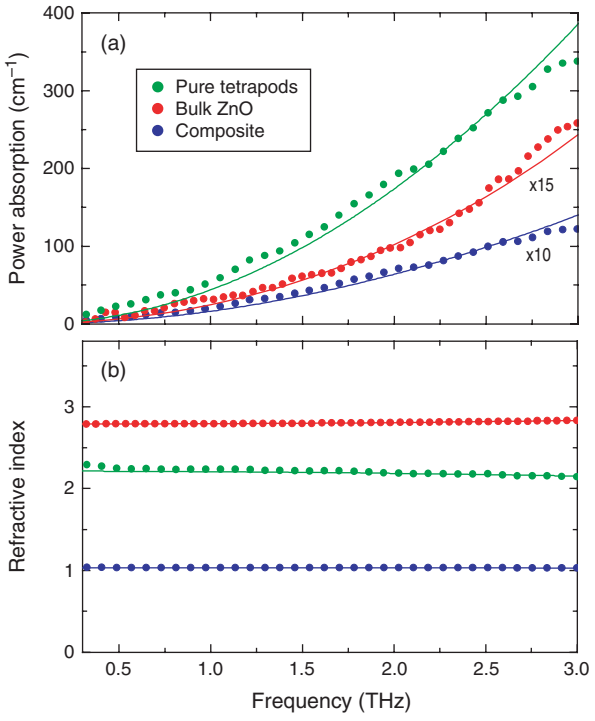

Fig. 9. Comparison of (a) measured power absorption, and (b) refractive index of pure ZnO tetrapods with that of bulk single-crystal ZnO and the tetrapod-air composite. The solid curves are corresponding theoretical fit to the data.

Nanostructures usually present a quite dissimilar optical property from bulk materials due to their high surface-to-volume ratio or their drastic changes in electron structures. Quantum confinement effects are often expected and observed in nanostructures. However, our THz-TDS study has shown that the THz spectra of ZnO tetrapods are similar with that of bulk single-crystal ZnO. This implies that the ZnO tetrapods preserve almost the overall crystal structure of the bulk ZnO. This result is also consistent with that of ZnO nanoparticles and ZnO nanotubes. When the radius of the nanostructures approaches the Bohr radius of exciton, the quantum confinement effect will become noticeable. The diameter of the legs in ZnO tetrapods is between 200 and 800 nm, much larger than the Bohr radius of ZnO (the calculated value is about 2 nm). This is why there are no obvious distinctions observed in dielectric properties between the single-crystal ZnO and tetrapod structures.

4.2.2. ZnS Nanoparticles

To prepare the ZnS nanoparticles, a four-neck flask was charged with 100 ml deionized water, 0.5 g polyvinyl alcohol and was stirred under N_2 for 1.5 h. An aqueous solution of 1.6 g Na_2S and an aqueous solution of 6 g $Zn(NO_3)_26(H_2O)$ were prepared and added to the first solution simultaneously via two different necks at the same rate.[34] After the addition, the resulting solution was stirred constantly under N_2 at 80 °C for 5 h and a transparent colloid of ZnS was formed. The nanoparticles were separated from solution by centrifugation and then dried in vacuum at 50 °C. The identity, crystallinity, crystal structure and size of the nanoparticles were examined by powder X-ray diffraction (XRD) which was recorded on an INEL diffractometer using a CPS 120 detector and a monochromatized $CuK_{\alpha 1}$ ($\lambda = 1.54056$ Å) radiation with Si ($a = 0.543088$ nm) as an internal standard. The XRD measurements demonstrate that the particles prepared have the zinc-blende structure (sphalerite). The broad XRD lines are indicative of the small size of ZnS nanoparticles. From the Debye-Scherrer equation, the average size of the ZnS nanoparticle sample is estimated to be around 3 nm.

The measured frequency-dependent power absorption and refractive index are plotted in Figures 10(a and b), respectively, in the frequency range of 0.3–3.0 THz.[34] As can be seen, the power absorption increases with increasing frequencies, whereas the refractive index n_r approaches a constant 1.5. No prominent absorption peaks

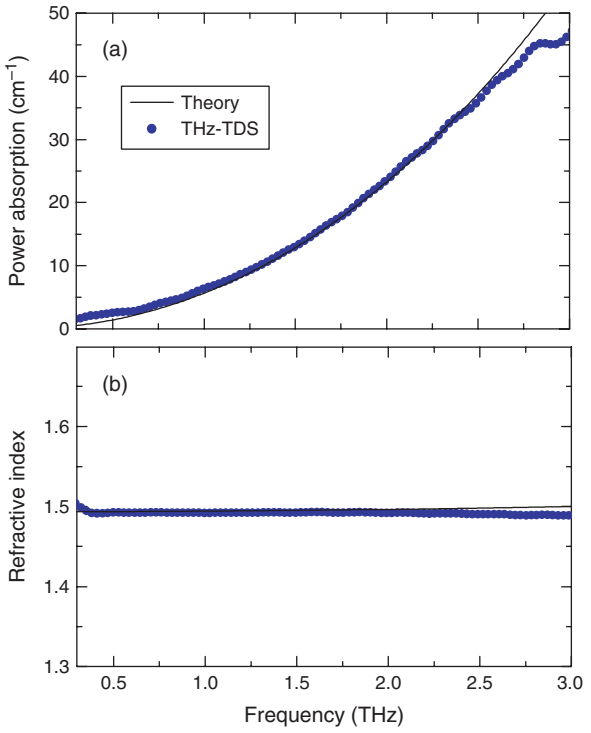

Fig. 10. (a) THz-TDS measured power absorption α and the theoretical fit based on the simple EMA model of ZnS nanoparticles; (b) measured refractive index and the theoretical fitting.

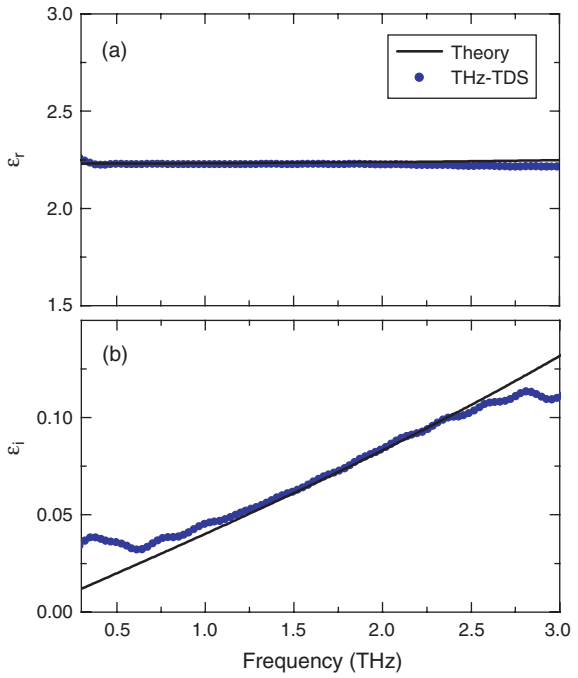

Fig. 11. Complex dielectric constant of ZnS nanoparticles: (a) measured real part of dielectric constant ε_r and the theoretical fitting; (b) measured imaginary dielectric constant ε_i and the theoretical fitting.

are observed below 3.0 THz, indicating that no remarkable change occurs in the refractive index. The frequency-dependent effective complex dielectric response of ZnS nanoparticles is determined by the recorded data of power absorption and refractive index as shown in Figures 11(a and b).[34] The characteristic response of ZnS nanoparticles was theoretically analyzed by combining the simple EMT model of Eqs. (9) and (6).

As shown in Figures 10 and 11, the measured power absorption, index of refraction, and the corresponding complex dielectric constant are well reproduced for $\varepsilon_h = 1.0$, $f = 0.3$, $\varepsilon_\infty = 3.0$, $\varepsilon_{st} = 2.10$, $\omega_{TO}/2\pi = 11.60$ THz and $\gamma/2\pi = 8.50$ THz. The good agreement between the measured data and the fitting indicates the presence of a dominant TO-phonon resonance centered at $\omega_{TO}/2\pi = 11.60$ THz with a linewidth of $\gamma/2\pi = 8.50$ THz and a strength $\varepsilon_{st} = 2.10$. Such a TO phonon resonance is quite consistent with the previously reported characteristic vibration frequency 11.6 ± 0.4 THz.[54] In comparison, this value is greater than the characteristic phonon frequency of bulk ZnS 7.12 ± 1.2 THz.

As mentioned above, the optical properties of nanoparticles can differ from those of their single crystal or bulk form due to surface effect of the finite size nanoparticles. Hence, it is essential to compare the THz spectroscopic response of ZnS nanoparticles with that of bulk single-crystal ZnS. Figure 12 shows a comparison of the experimentally extracted power absorption and refractive index of bulk single-crystal ZnS with that of ZnS nanoparticles.[30, 34] Clearly, the bulk single-crystal ZnS shows lower absorption, but relatively high refractive index. In addition, two prominent phonon resonances

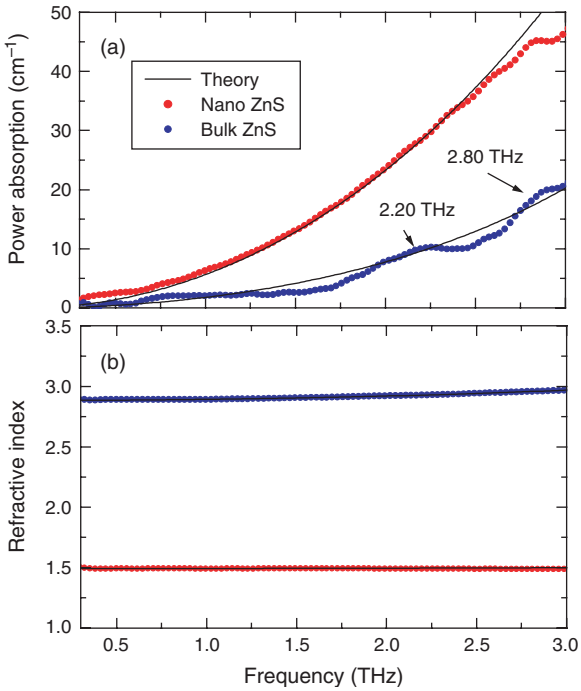

Fig. 12. Comparison of measured power absorption and refractive index of ZnS nanoparticles with that of bulk single-crystal ZnS.

located at 2.20 and 2.80 THz are observed as a further distinction of bulk single-crystal ZnS for the nanoparticles. These characteristic phonon frequencies are assigned to TA(L) = 73 cm^{-1} (2.2 THz) and TA(X) = 93 cm^{-1} (2.8 THz), respectively.[55] The consistent fit on the measured data indicates that a TO phonon resonance is localized at 8.13 THz.

Generally, the optical phonon resonances of particles shift to higher frequencies as the particle size decreases. For optical phonons in nonpolar microcrystals, such as Si and Ge, the size-dependent shift and broadening were commonly observed. In addition, the Raman peak of Ag particles was observed to shift to higher frequency with decreasing particle size. These features provide a qualitative explanation of our measurements that the TO frequency of ZnS nanoparticles is higher than that of single-crystal ZnS. Moreover, combining with the fact showing below, we would justify that such a feature is also associated with the surface effect of ZnS nanoparticles. It is interesting that the phonon modes of single-crystal ZnS at 2.2 and 2.8 THz are not found in the spectra of ZnS nanoparticles.

For ionic crystalline solids such as single-crystal ZnS, the atoms are bound in periodic arrays which propagate waves with constraints and behavior imposed by the dynamics of lattice motion. The interaction of a radiation field with the fundamental lattice vibrations generally results in absorption of electromagnetic waves due to the creation or annihilation of lattice vibrations. Optical absorption of ionic crystals in the far-infrared region can be ascribed to the lattice vibration, which includes many modes induced by the interaction between metal ions and anions, as well as interaction between metal ions and between anions. However, as discussed above, the surface-to-volume ratio of nanoparticles is very large and the number of atoms on the surface is comparable to or larger than that inside the particles. The absorption is mainly ascribed to the contribution of the surface of particles. Therefore, it is not surprising that not all resonance modes of bulk ZnS are observed in ZnS nanoparticles. The experimental results clearly clarify that the acoustic phonons become confined in small-size nanoparticles compared to bulk materials. Due to the localization of acoustic vibrational motion, both the TA(L) and the TA(X) modes in single-crystal ZnS are not observed in ZnS nanoparticles. Our measurements are also in good agreement with the previous experimental work.[56, 57]

5. CONCLUSIONS

Wide-bandgap semiconductors are promising in THz optoelectronics applications, particularly in high power THz generation due to high break-down field, rather high mobility, and low absorption in broad THz frequency range. The far-infrared optical, dielectric, or electric response of selected crystalline and nanostructured wide-bandgap semiconductors has been reviewed. The frequency-dependent electron dynamics, power absorption, and optical dispersion of a free-standing, crystalline GaN were presented over a broad THz spectral range. The measured conductivity was well fit by the Drude model, indicating that the THz optical response of the unintentionally *n*-doped GaN is highly related to the contribution from free electrons or plasmons. The THz-TDS determined optical and dielectric properties of high-resistivity, single-crystal ZnO was well fit by the pseudo-harmonic model of dielectric response. The extrapolation of the experimental data has shown that the dielectric characteristics of bulk ZnO is dominated by the transverse optical E_1 (TO (E_1)) phonon mode centered at ($\omega_{TO}/2\pi$) 12.42 THz. The nanostructured ZnO tetrapods have revealed a similar optical response as that of bulk ZnO for their dielectric response was also associated with the transverse optical E_1 (TO (E_1)) phonon mode. The studies on ZnS single-crystal and nanoparticle samples indicate that the characteristic phonon resonance of ZnS nanoparticles is dominated by the TO phonon at 11.6 THz. This characteristic phonon frequency is higher than that of single-crystal ZnS at 7.8 THz. It was noted that not all the phonon modes in single-crystal ZnS can be observed in nanostructures due to the confinement of acoustic phonons in ZnS nanoparticles.

Acknowledgments: The authors thank D. Grischkowsky, D. C. Look, J. Dai, M. He, S. L. Thamizhmani, S. Ray, W. Chen, S. H. Li, Y. Zhao, X. Lu, and Z. Zhu for their outstanding contributions and efforts in this research. It is a great honor for the authors to work collaboratively with them and to present their accomplishments. This work was partially supported by the National Science Foundation and the Oklahoma EPSCoR for the National Science Foundation. A. K. Azad is now with the Los Alamos National Laboratory.

References and Notes

1. T. C. McGill, C. M. S. Torres, and W. Gebhardt, Growth and Optical Properties of Wide-Gap II–VI Low-Dimensional Semiconductors, Plenum Press, New York **(1989)**, Part I, pp. 1–65.
2. J. Y. Sohn, J. S. Yahng, D. J. Park, E. Oh, D. S. Kim, G. D. Sanders, C. J. Stanton, and D. S. Citrin, Technical Digest of QELS, Long Beach, USA **(2002)**.
3. S. Ono, H. Murakami, A. Quema, G. Diwa, N. Sarukura, R. Nagasaka, Y. Ichikawa, E. Oshima, H. Ogino, A. Yoshikawa, and T. Fukuda, Technical Digest of CLEO, Baltimore, USA **(2005)**.
4. T. Hattori, Y. Homma, A. Mitsuishi, and M. Tacke, *Opt. Commun.* 7, 229 **(1973)**.
5. D. C. Reynolds, D. C. Look, B. Jogai, A. W. Saxler, S. S. Park, and J. Y. Hahn, *Appl. Phys. Lett.* 77, 2879 **(2000)**.
6. D. C. Reynolds, B. Jogai, and T. C. Collins, *Appl. Phys. Lett.* 80, 3928 **(2002)**.
7. A. Kasic, M. Schubert, S. Einfeldt, D. Hommel, and T. E. Tiwald, *Phys. Rev. B* 62, 7365 **(2000)**.

8. A. Yasan, R. McClintock, K. Mayes, S. R. Darvish, H. Zhang, P. Kung, M. Razeghi, S. K. Lee, and J. Y. Han, *Appl. Phys. Lett.* 81, 2151 **(2002)**.

9. W. J. Moore, J. A. Freitas, Jr., S. K. Lee, S. S. Park, and J. Y. Han, *Phys. Rev. B* 65, 081201 **(2002)**.

10. D. D. Chen, M. Smith, J. Y. Lin, H. X. Jiang, S. H. Wei, M. A. Khan, and C. J. Sun, *Appl. Phys. Lett.* 68, 2784 **(1996)**.

11. W. Zhang, A. K. Azad, and D. Grischkowsky, *Appl. Phys. Lett.* 82, 2841 **(2003)**.

12. T. Nagashima, K. Takata, and S. Nashima, et al., *Jap. J. Appl. Phys. Part 1* 44, 926 **(2005)**.

13. V. Srikant and D. R. Clarke, *J. Appl. Phys.* 83, 5447 **(1998)**.

14. Z. K. Tang, G. K. L. Wong, P. Yu, M. Kawasaki, A. Ohtomo, H. Koinuma, and Y. Segawa, *Appl. Phys. Lett.* 72, 3270 **(1998)**.

15. D. M. Bagnall, Y. F. Chen, Z. Zhu, T. Yao, S. Koyama, M. Y. Shen, and T. Goto, *Appl. Phys. Lett.* 70, 2230 **(1997)**.

16. N. Ashkenov, B. N. Mbenkum, C. Bundesmann, V. Riede, M. Lorenz, D. Spemann, E. M. Kaidashev, A. Kasic, M. Schubert, M. Grundmann, G. Wagner, H. Neumann, V. Darakchieva, H. Arwin, and B. Monemar, *J. Appl. Phys.* 93, 126 **(2003)**.

17. D. C. Look, D. C. Reynolds, J. W. Hemsky, R. L. Jones, and J. R. Sizelove, *Appl. Phys. Lett.* 75, 811 **(1999)**.

18. A. K. Azad, J. G. Han, and W. Zhang, *Appl. Phys. Lett.* 88, 021103 **(2006)**.

19. Z. R. Tian, J. A. Voigt, J. Liu, B. Mckenzie, M. J. McDermott, M. A. Rodriguez, H. Kngishi, and H. Xu, *Nature Mater.* 2, 821 **(2003)**.

20. V. A. L. Roy, A. B. Djurisic, W. K. Chan, J. Gao, H. F. Lui, and C. Surya, *Appl. Phys. Lett.* 83, 141 **(2003)**.

21. R. Wu, J. Wu, C. Xie, X. Zhang, and A. Wang, *Mater. Sci. Eng. A* 328, 196 **(2002)**.

22. X. Chu, D. Jiang, B. A. Djurisic, and H. Y. Leung, *Chem. Phys. Lett.* 401, 426 **(2005)**.

23. V. A. L. Roy, A. B. Djurisic, H. Liu, X. X. Zhang, Y. H. Leung, M. H. Xie, J. Gao, H. F. Lui, and C. Surya, *Appl. Phys. Lett.* 84, 756 **(2004)**.

24. B. Y. Geng, L. D. Zhang, G. Z. Wang, T. Xie, Y. G. Zhang, and G. W. Meng, *Appl. Phys. Lett.* 84, 2157 **(2004)**.

25. S. Gupta, S. J. Meclure, and V. P. Singh, *Thin Solid Films* 299, 33 **(1997)**.

26. A. D. Yoffe, *Adv. Phys.* 50, 1 **(2001)**.

27. S. W. Haggata, X. Li, D. J. Cole-Hamilton, and J. R. Fryer, *J. Mater. Chem.* 6, 1771 **(1996)**.

28. J. Xu, H. Mao, Y. Sun, and Y. Du, *J. Vac. Sci. Technol. B* 15, 1465 **(1997)**.

29. D. Grischkowsky, S. Keiding, M. Van Exter, and Ch. Fattinger, *J. Opt. Soc. Am. B* 7, 2006 **(1990)**.

30. L. Thamizhmani, A. K. Azad, J. Dai, and W. Zhang, *Appl. Phys. Lett.* 86, 131111 **(2005)**.

31. M. Grynberg, R. Le Toullec, and M. Balkanski, *Phys. Rev. B* 9, 517 **(1974)**.

32. F. Abelès (ed.), Optical Properties of Solids, North-Holland, New York **(1972)**, Chap. 8, pp. 529–530.

33. J. Han, F. Wan, Z. Zhu, Y. Liao, T. Ji, M. Ge, and Z. Zhang, *Appl. Phys. Lett.* 87, 172107 **(2005)**.

34. J. Han, W. Zhang, W. Chen, L. Thamizhmani, A. K. Azad, and Z. Zhu, *J. Phys. Chem. B* 110, 1989 **(2006)**.

35. M. Fujii, M. Wada, S. Kayashi, and K. Yamamoto, *Phys. Rev. B* 46, 15930 **(1992)**.

36. C. G. Granqvist and O. Hunderi, *Phys. Rev. B* 18, 2897 **(1978)**.

37. H. Weissker, J. Furthmuller, and F. Bechstedt, *Phys. Rev. B* 67, 165322 **(2003)**.

38. M. Born and E. Wolf, Principles of Optics, 7th (expanded) edn., Cambridge University Press, Cambridge, UK **(2002)**, Chap. 1, pp. 65–66.

39. O. Madelung (ed.), Physics of II–VI and I–VII Compounds, Semimagnetic Semiconductors, Springer-Verlag, Berlin **(1982)**.

40. C. A. Arguello, D. L. Rousseau, and S. P. S. Porto, *Phys. Rev.* 181, 1351 **(1969)**.

41. T. C. Damen, S. P. S. Porto, and B. Tell, *Phys. Rev.* 142, 570 **(1966)**.

42. S. S. Mitra and R. Marshall, *Proceedings of the International Conference on the Physics of Semiconductors*, Academic, New York **(1965)**.

43. R. J. Collins and D. A. Kleinman, *J. Phys. Chem. Solids* 11, 190 **(1959)**.

44. F. Decremps, J. Pellicer-Porres, A. M. Saitta, J.-C. Chervin, and A. Polian, *Phys. Rev. B* 65, 092101 **(2002)**.

45. J. M. Calleja and M. Cardona, *Phys. Rev. B* 16, 3753 **(1977)**.

46. W. G. Nilsen, *Phys. Rev.* 182, 838 **(1969)**.

47. G. A. Slack and S. Roberts, *Phys. Rev. B* 3, 2613 **(1971)**.

48. L. Feldkamp, G. Venkataraman, and J. S. King, *Solid State Commun.* 7, 1571 **(1969)**.

49. J. Bergsma, *Phys. Lett. A* 32, 324 **(1970)**.

50. N. Vagelatos, D. Wehe, and J. S. King, *J. Chem. Physics* 60, 3613 **(1974)**.

51. C. A. Klein and R. N. Donadio, *J. Appl. Phys.* 51, 797 **(1980)**.

52. G. Gallot, J. Zhang, R. W. McGowan, T. I. Jeon, and D. Grischkowsky, *Appl. Phys. Lett.* 74, 3450 **(1999)**.

53. J. Han, Z. Zhu, S. Ray, A. Azad, W. Zhang, M. He, S. Li, and Y. Zhao, *Appl. Phys. Lett.* 89, 031107 **(2006)**.

54. B. Gilbert, F. Huang, H. Zhang, G. A. Waychunas, and J. F. Banfield, *Science* 305, 651 **(2004)**.

55. R. Marschall and S. Mitra, *Phys. Rev. A* 134, 1019 **(1964)**.

56. S. Nomura and T. Kobayashi, *Solid State Commun.* 82, 335 **(1992)**.

57. G. Cerullo, S. D. Silvestr, and U. Banin, *Phys. Rev. B* 60, 1928 **(1999)**.

Received: 15 May 2007. Revised/Accepted: 4 September 2007.